

Article

Effect of Cu Substitution and Heat Treatment on Phase Formation and Magnetic Properties of $\text{Sm}_{12}\text{Co}_{88-x}\text{Cu}_x$ Melt-Spun Ribbons

Feilong Dai ¹, Peipei Liu ¹, Lin Luo ¹, Dekang Chen ¹, Qingrong Yao ^{1,2} and Jiang Wang ^{1,2,*}

¹ Guangxi Key Laboratory of Information Materials, School of Materials Science and Engineering, Guilin University of Electronic Technology, Guilin 541004, China; daifeilong190@163.com (F.D.); lpp656357819@163.com (P.L.); luolin152@163.com (L.L.); chendekang181@163.com (D.C.); qingry96@guet.edu.cn (Q.Y.)

² Engineering Research Center of Electronic Information Materials and Devices, Ministry of Education, Guilin University of Electronic Technology, Guilin 541004, China

* Correspondence: wangjiang158@163.com or waj124@guet.edu.cn

Abstract: The phase structure and microstructure of $\text{Sm}_{12}\text{Co}_{88-x}\text{Cu}_x$ ($x = 0, 2, 4, 6, 8, 10$; at.%) as-cast alloys and melt-spun ribbons prepared via the arc-melting method and melt-spun technology were studied experimentally by X-ray diffraction (XRD) and scanning electron microscope (SEM) with energy dispersive spectroscopy (EDS). The results reveal that the $\text{Sm}_{12}\text{Co}_{88-x}\text{Cu}_x$ ($x = 0$) as-cast alloy contains $\text{Sm}_2\text{Co}_{17}$ and $\text{Sm}_5\text{Co}_{19}$ phases, while the $\text{Sm}_{12}\text{Co}_{88-x}\text{Cu}_x$ ($x = 2$) as-cast alloy is composed of $\text{Sm}_2\text{Co}_{17}$, Sm_2Co_7 and $\text{Sm}(\text{Co}, \text{Cu})_5$ phases. $\text{Sm}_2\text{Co}_{17}$ and $\text{Sm}(\text{Co}, \text{Cu})_5$ phases are detected in $\text{Sm}_{12}\text{Co}_{88-x}\text{Cu}_x$ ($x = 4, 6, 8, 10$) as-cast alloys. Meanwhile, $\text{Sm}_{12}\text{Co}_{88-x}\text{Cu}_x$ ribbons show a single SmCo_7 phase, which is still formed in the ribbons annealed at 1023 K for one hour. After annealed at 1123 K for two hours, cooled slowly down to 673 K at 0.5 K/min and then kept for four hours, the ribbons are composed of $\text{Sm}_2\text{Co}_{17}$ and $\text{Sm}(\text{Co}, \text{Cu})_5$ phases. The magnetic measurements of $\text{Sm}_{12}\text{Co}_{88-x}\text{Cu}_x$ ribbons were performed by vibrating sample magnetometer (VSM). The results exhibit that the maximum magnetic energy product $((\text{BH})_{\text{max}})$, the coercivity (H_{cj}) and the remanence (B_{r}) of the $\text{Sm}_{12}\text{Co}_{88-x}\text{Cu}_x$ ribbons increase generally with the increase in Cu substitution. In particular, the magnetic properties of the ribbons annealed at 1123 K and 673 K increase significantly with the increase in Cu substitution, resulting from the increase in the volume fraction of the formed $\text{Sm}(\text{Co}, \text{Cu})_5$ phase after heat treatment.



Citation: Dai, F.; Liu, P.; Luo, L.; Chen, D.; Yao, Q.; Wang, J. Effect of Cu Substitution and Heat Treatment on Phase Formation and Magnetic Properties of $\text{Sm}_{12}\text{Co}_{88-x}\text{Cu}_x$ Melt-Spun Ribbons. *Materials* **2022**, *15*, 4494. <https://doi.org/10.3390/ma15134494>

Academic Editors: Aleksandra Kolano-Burian and Lukasz Hawelek

Received: 13 May 2022

Accepted: 23 June 2022

Published: 25 June 2022

Publisher's Note: MDPI stays neutral with regard to jurisdictional claims in published maps and institutional affiliations.



Copyright: © 2022 by the authors. Licensee MDPI, Basel, Switzerland. This article is an open access article distributed under the terms and conditions of the Creative Commons Attribution (CC BY) license (<https://creativecommons.org/licenses/by/4.0/>).

Keywords: Sm-Co-Cu; melt-spun ribbons; phase structure; magnetic properties

1. Introduction

Sm-Co-based permanent magnets have been used in aerospace, electric vehicle motors, wind turbines, sensors and actuators because of high Curie temperatures, excellent temperature stability and good corrosion resistance [1–3]. Extensive investigations were conducted to investigate the magnetic properties of Sm-Co alloys with alloying elements Fe, Cu and Zr, which results in a new class of $\text{Sm}(\text{Co}, \text{Fe}, \text{Cu}, \text{Zr})_z$ ($5 \leq Z \leq 8.5$) permanent magnets [4–11]. It was reported that the addition of Cu into Sm-Co-based permanent magnets would improve their coercivity (H_{cj}) [12–18]. Tellez-Blanco et al. [14] found that the coercivity of $\text{SmCo}_{0.5-x}\text{Cu}_x$ annealed alloys increases and then decreases with the increase in Cu substitution. Horiuchi et al. [15] reported the $(\text{BH})_{\text{max}}$ of $\text{Sm}(\text{Co}_{\text{bal}}\text{Fe}_{0.35}\text{Cu}_{0.06}\text{Zr}_{0.018})_{7.8}$ magnet is 32 MGOe. Subsequently, Horiuchi et al. [16] further improved the H_{cj} and $(\text{BH})_{\text{max}}$ of $\text{Sm}(\text{Co}_{\text{bal}}\text{Fe}_{0.35}\text{Cu}_{0.06}\text{Zr}_{0.018})_{7.8}$ magnet by means of process optimization. Wang et al. [17] found that the H_{cj} of $\text{Sm}(\text{Co}_{0.665}\text{Fe}_{0.25}\text{Cu}_{0.06}\text{Zr}_{0.025})_7$ magnet increases significantly from 12 kOe to 21 kOe. Xu et al. [18] investigated the effect of heat treatment on the formation of 1:5H cell wall phase in 2:17 type melt-spun ribbons with high Fe content. It was detected

that the Cu content is the key to the formation of the 1:5H cell wall phase, which would improve the magnetic properties of the 2:17 type melt-spun ribbons with high Fe content.

Therefore, in order to further understand the effect of Cu substitution and heat treatment on the magnetic properties of Sm-Co alloys, the phase formation, microstructure and magnetic properties of $\text{Sm}_{12}\text{Co}_{88-x}\text{Cu}_x$ alloys were investigated in this work by X-ray diffraction (XRD), scanning electron microscope (SEM) with energy dispersive spectroscopy (EDS) and vibrating sample magnetometer (VSM).

2. Experimental Procedure

$\text{Sm}_{12}\text{Co}_{88-x}\text{Cu}_x$ ($x = 0, 2, 4, 6, 8, 10$; at.%) alloys were fabricated through arc-melting method using bulk Sm, Co and Cu metals (99.99% purity) as the raw materials. The as-cast alloys were melted four times during the arc-melting process to ensure composition homogeneity. The ribbons were acquired by induction melting as-cast alloys and then spraying the melts through the orifice (orifice diameter approximately 0.8–1.0 mm) onto the copper wheel surface at the wheel speed of 40 m/s. The thickness and the width of the melt-spun ribbons are about 10–15 μm and 2–3 mm, respectively. The ribbons were sealed in quartz tubes filled with high pure argon gas. After heat treatment, the quartz tubes with the ribbons were quenched in ice water. In this work, the first heat-treatment was that the ribbons were annealed at 1023 K for 1 h, while the second heat-treatment was that the ribbons were annealed at 1123 K for 2 h, and then were slowly cooled down to 673 K at 0.5 K/min and kept at 673 K for 4 h.

The phase structure, phase composition and microstructure of as-cast alloys and melt-spun ribbons were analyzed by X-ray powder diffraction (XRD, PLXcel 3D, Cu $K\alpha$ radiation) and scanning electron microscope with energy dispersive spectroscopy (SEM-EDS, FEI 450G). The lattice parameters and volume fractions of the formed phases in as-cast alloys and the ribbons were determined by the Rietveld refinements with the Fullprof program. The magnetic properties of the ribbons are measured at room temperature via vibrating sample magnetometer (VSM, Lakeshore Model 7400 740H). In this work, the demagnetization correction of the ribbons is neglected because the applied external field is parallel to the plane of the ribbons in the magnetic measurements.

3. Results and Discussion

3.1. Phase Formation

Figure 1a is the Rietveld refinements of XRD powder patterns of $\text{Sm}_{12}\text{Co}_{88-x}\text{Cu}_x$ ($x = 0, 2, 4, 6, 8, 10$) as-cast alloys. As can be seen in Figure 1a, the red points and solid lines show the experimental and calculated XRD patterns of the as-cast alloys, respectively. The vertical bars indicate Bragg reflection positions. The green lines show the differences between the experimental and computed intensities. Based on the agreement factor (R_{wp}), the calculated patterns are consistent with the experimental patterns. On the basis of the Rietveld refinements in Figure 1a, the $\text{Sm}_{12}\text{Co}_{88-x}\text{Cu}_x$ ($x = 0$) as-cast alloy shows $\text{Sm}_2\text{Co}_{17}$ and $\text{Sm}_5\text{Co}_{19}$ phases, while the $\text{Sm}_{12}\text{Co}_{88-x}\text{Cu}_x$ ($x = 2$) as-cast alloy is composed of $\text{Sm}_2\text{Co}_{17}$, Sm_2Co_7 and $\text{Sm}(\text{Co}, \text{Cu})_5$ phases, and the $\text{Sm}_{12}\text{Co}_{88-x}\text{Cu}_x$ ($x = 4, 6, 8, 10$) as-cast alloys consist of $\text{Sm}_2\text{Co}_{17}$ and $\text{Sm}(\text{Co}, \text{Cu})_5$ phases. Table 1 shows the lattice parameters and the cell volume of the $\text{Sm}_2\text{Co}_{17}$ phase in $\text{Sm}_{12}\text{Co}_{88-x}\text{Cu}_x$ as-cast alloys obtained finally by the Rietveld refinements. As can be seen from Figure 1b, except for the $\text{Sm}_{12}\text{Co}_{88-x}\text{Cu}_x$ ($x = 2$) as-cast alloy, the lattice parameters and cell volume of the $\text{Sm}_2\text{Co}_{17}$ phase in the $\text{Sm}_{12}\text{Co}_{88-x}\text{Cu}_x$ as-cast alloy increase linearly with the increase in Cu substitution. It means that Cu atoms with the larger radii enter into the structure lattice of the $\text{Sm}_2\text{Co}_{17}$ phase for replacing Co atoms in the $\text{Sm}_{12}\text{Co}_{88-x}\text{Cu}_x$ as-cast alloys. However, the lattice parameters and the cell volumes of the $\text{Sm}_2\text{Co}_{17}$ phases in the $\text{Sm}_{12}\text{Co}_{88-x}\text{Cu}_x$ ($x = 2$) as-cast alloy are abnormally larger than those in the samples with more Cu substitution. Guo et al. [19] and Chang et al. [20] showed that Cu atoms tend to occupy the 3g crystal site in RE/(Co, M) structures, and there are much more Sm atoms on the 3g crystal site. Thus, the abnormal increase in the lattice parameters of the $\text{Sm}_2\text{Co}_{17}$ phase in the $\text{Sm}_{12}\text{Co}_{88-x}\text{Cu}_x$ ($x = 2$) as-cast

alloy may be caused by the substitution of Sm by Cu at the 3g crystal site. The peak of the $\text{Sm}(\text{Cu},\text{Co})_5$ phase in the $\text{Sm}_{12}\text{Co}_{88-x}\text{Cu}_x$ ($x = 2$) as-cast alloy (near 36°) migrates a little compared with other samples. This may be because Co-Co atom pairs replace part of the Sm atoms. Since the atomic radii of the Co-Co atom pairs are larger than those of the Sm atoms, the diffraction peaks of the $\text{Sm}(\text{Cu},\text{Co})_5$ phase in the $\text{Sm}_{12}\text{Co}_{88-x}\text{Cu}_x$ ($x = 2$) as-cast alloy shift slightly to lower 2θ values. This phenomenon was introduced by Yuan et al. [21].

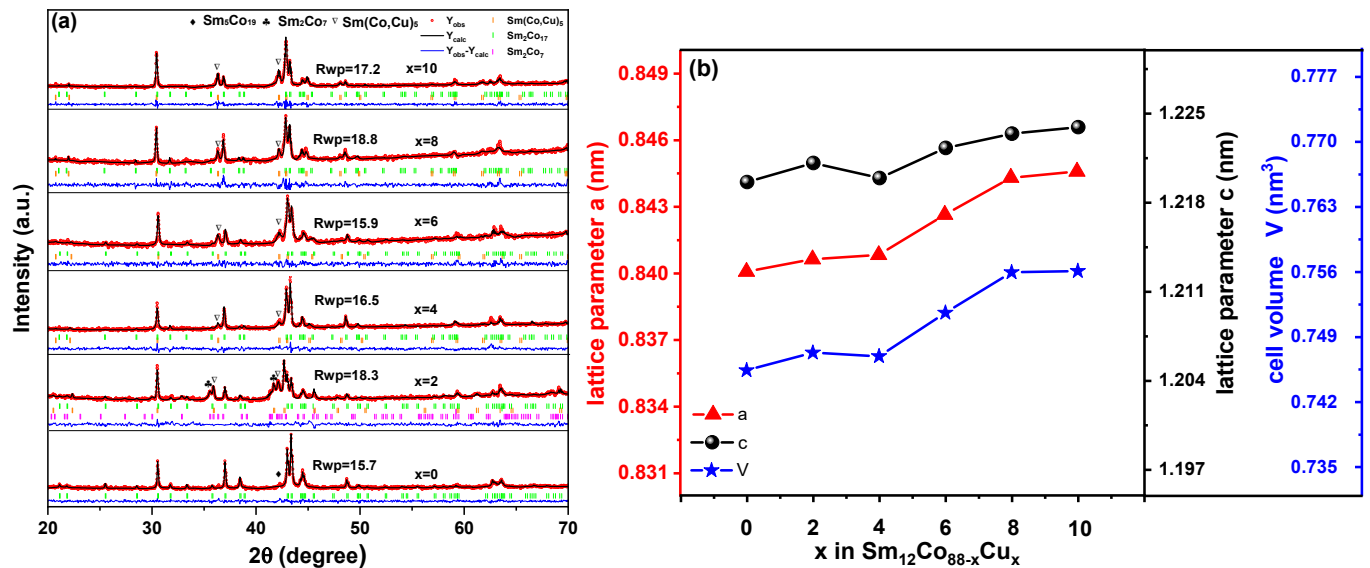


Figure 1. (a) Rietveld refinements of XRD patterns of $\text{Sm}_{12}\text{Co}_{88-x}\text{Cu}_x$ ($x = 0, 2, 4, 6, 8, 10$) as-cast alloys and (b) the lattice parameters and cell volume of $\text{Sm}_2\text{Co}_{17}$ phase in $\text{Sm}_{12}\text{Co}_{88-x}\text{Cu}_x$ ($x = 0, 2, 4, 6, 8, 10$) as-cast alloys.

Table 1. Lattice parameters, cell volume and volume fraction of the formed phases in $\text{Sm}_{12}\text{Co}_{88-x}\text{Cu}_x$ alloys by Rietveld refinements.

$\text{Sm}_{12}\text{Co}_{88-x}\text{Cu}_x$ Alloys	x	Lattice Parameters						Volume Fractions			
		$\text{Sm}_2\text{Co}_{17}$			SmCo_7			$\text{Sm}_2\text{Co}_{17}$	$\text{Sm}(\text{Co}, \text{Cu})_5$	Sm_2Co_7	SmCo_7
		a (Å)	c (Å)	Volume (Å ³)	a (Å)	c (Å)	Volume (Å ³) (Å ³)	(%)	(%)	(%)	(%)
As cast alloys	0	8.400 (8)	12.196 (2)	745.417 (2)	—	—	—	100	—	—	—
	2	8.406 (4)	12.211 (2)	747.321 (6)	—	—	—	88.7	2.3	9.0	—
	4	8.408 (3)	12.199 (4)	746.931 (9)	—	—	—	85.2	14.8	—	—
	6	8.426 (5)	12.223 (0)	751.626 (2)	—	—	—	81.5	18.5	—	—
	8	8.443 (1)	12.234 (2)	755.958 (6)	—	—	—	79.3	21.7	—	—
	10	8.445 (9)	12.239 (3)	756.100 (0)	—	—	—	78.2	22.8	—	—
Melt-spun ribbons	0	—	—	—	4.857 (8)	4.069 (9)	83.173 (8)	—	—	—	100
	2	—	—	—	4.905 (6)	4.047 (6)	84.355 (0)	—	—	—	100
	4	—	—	—	4.847 (7)	4.080 (6)	83.048 (5)	—	—	—	100
	6	—	—	—	4.880 (1)	4.067 (6)	83.895 (4)	—	—	—	100
	8	—	—	—	4.871 (7)	4.076 (5)	83.789 (3)	—	—	—	100
	10	—	—	—	4.872 (9)	4.070 (7)	83.711 (4)	—	—	—	100
Melt-spun ribbons annealed at 1023 K	0	—	—	—	4.867 (2)	4.067 (6)	83.450 (2)	—	—	—	100
	2	—	—	—	4.905 (4)	4.047 (9)	84.353 (3)	—	—	—	100
	4	—	—	—	4.870 (0)	4.068 (5)	83.565 (4)	—	—	—	100
	6	—	—	—	4.868 (7)	4.068 (3)	83.515 (7)	—	—	—	100
	8	—	—	—	4.912 (8)	4.066 (2)	84.991 (1)	—	—	—	100
	10	—	—	—	4.873 (6)	4.070 (5)	83.729 (6)	—	—	—	100

Table 1. Cont.

Sm ₁₂ Co _{88-x} Cu _x Alloys	x	Lattice Parameters						Volume Fractions			
		Sm ₂ Co ₁₇			SmCo ₇			Sm ₂ Co ₁₇	Sm(Co, Cu) ₅	Sm ₂ Co ₇	SmCo ₇
		a (Å)	c (Å)	Volume (Å ³)	a (Å)	c (Å)	Volume (Å ³) (Å ³)	(%)	(%)	(%)	(%)
	0	8.408 (2)	12.200 (7)	746.992 (6)	—	—	—	100	—	—	—
Melt-spun ribbons annealed at 1123 K and 673 K	2	8.416 (4)	12.208 (3)	748.920 (2)	—	—	—	100	—	—	—
	4	8.401 (6)	12.217 (6)	746.866 (6)	—	—	—	95.1	4.9	—	—
	6	8.410 (2)	12.210 (4)	747.948 (4)	—	—	—	93.4	6.6	—	—
	8	8.428 (4)	12.222 (8)	751.961 (7)	—	—	—	88.6	11.4	—	—
	10	8.435 (4)	12.223 (9)	752.855 (4)	—	—	—	84.2	15.8	—	—

Figure 2 displays the backscattered electron (BSE) images of Sm₁₂Co_{88-x}Cu_x (x = 0, 2, 4, 6, 8, 10) as-cast alloys. The phase compositions of the formed phases in Sm₁₂Co_{88-x}Cu_x as-cast alloys were measured by EDS as shown in Table 2. In Figure 2a, there are two phases in the microstructure of the Sm₁₂Co_{88-x}Cu_x (x = 0) as-cast alloy. The white phase is the Sm₅Co₁₉ phase, and the gray phase is the Sm₂Co₁₇ phase based on the EDS measurements in Table 2. It was stated clearly that the SEM-EDS results of Sm₁₂Co_{88-x}Cu_x as-cast alloys are consistent with the XRD results, except for the Sm₅Co₁₉ phase in the Sm₁₂Co_{88-x}Cu_x (x = 0) as-cast alloy, which was not detected by the XRD analysis due to low volume fraction.

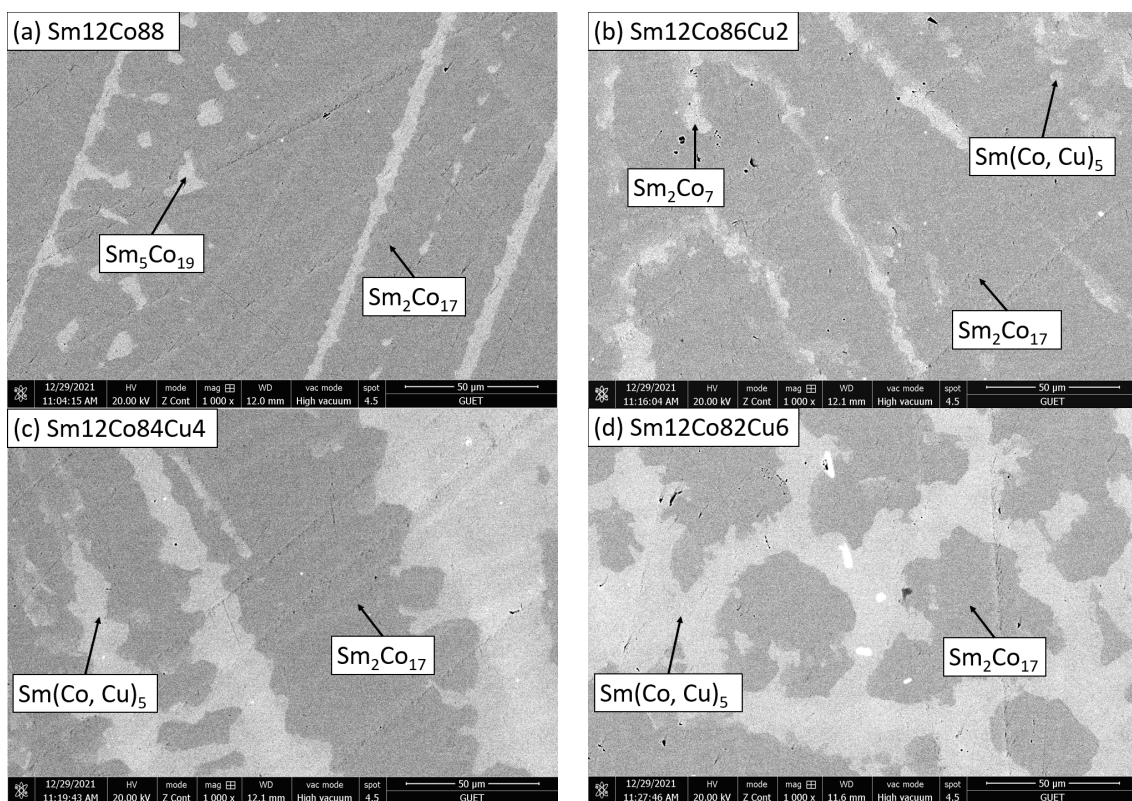


Figure 2. Cont.

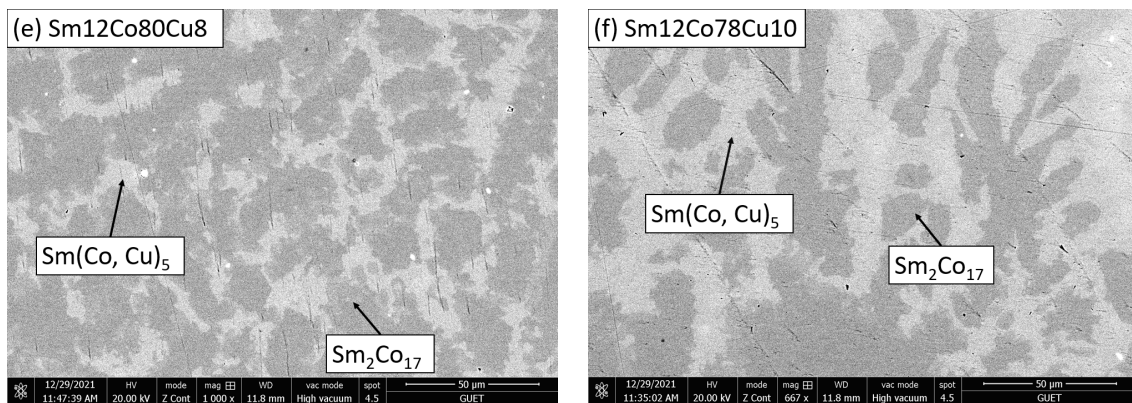


Figure 2. Backscattered electron (BSE) images of $\text{Sm}_{12}\text{Co}_{88-x}\text{Cu}_x$ as-cast alloys. (a) $x = 0$, (b) $x = 2$, (c) $x = 4$, (d) $x = 6$, (e) $x = 8$, (f) $x = 10$.

Table 2. Phase formation and phase composition of $\text{Sm}_{12}\text{Co}_{88-x}\text{Cu}_x$ as-cast alloys determined by EDS and XRD.

$\text{Sm}_{12}\text{Co}_{88-x}\text{Cu}_x$ As-Cast Alloys (at.%)	Composition Measured by EDS (at.%)				Phase	Phase Identified by XRD
	Sm	Co	Cu	Phase		
$x = 0$	20.13	78.87	0	$\text{Sm}_5\text{Co}_{19}$	$\text{Sm}_5\text{Co}_{19}$	
	11.23	88.77	0	$\text{Sm}_2\text{Co}_{17}$	$\text{Sm}_2\text{Co}_{17}$	
$x = 2$	21.58	77.19	1.23	Sm_2Co_7	Sm_2Co_7	
	14.16	84.19	1.65	$\text{Sm}(\text{Co}, \text{Cu})_5$	$\text{Sm}(\text{Co}, \text{Cu})_5$	
$x = 4$	10.69	88.18	1.12	$\text{Sm}_2\text{Co}_{17}$	$\text{Sm}_2\text{Co}_{17}$	
	15.78	80.40	3.82	$\text{Sm}(\text{Co}, \text{Cu})_5$	$\text{Sm}(\text{Co}, \text{Cu})_5$	
$x = 6$	11.62	85.65	2.73	$\text{Sm}_2\text{Co}_{17}$	$\text{Sm}_2\text{Co}_{17}$	
	15.78	79.27	4.98	$\text{Sm}(\text{Co}, \text{Cu})_5$	$\text{Sm}(\text{Co}, \text{Cu})_5$	
$x = 8$	11.05	83.63	5.32	$\text{Sm}_2\text{Co}_{17}$	$\text{Sm}_2\text{Co}_{17}$	
	16.23	76.65	7.12	$\text{Sm}(\text{Co}, \text{Cu})_5$	$\text{Sm}(\text{Co}, \text{Cu})_5$	
$x = 10$	11.39	82.34	6.27	$\text{Sm}_2\text{Co}_{17}$	$\text{Sm}_2\text{Co}_{17}$	
	16.32	75.22	8.46	$\text{Sm}(\text{Co}, \text{Cu})_5$	$\text{Sm}(\text{Co}, \text{Cu})_5$	
	11.22	81.65	7.13	$\text{Sm}_2\text{Co}_{17}$	$\text{Sm}_2\text{Co}_{17}$	

Figure 3 shows the calculated vertical section of 12 at.% Sm and volume fractions of the formed phases as a function of Cu concentration in the $\text{Sm}_{12}\text{Co}_{88-x}\text{Cu}_x$ as-cast alloys at 673 K, which were calculated with the thermo-Calc[®] software package using thermodynamic parameters of the Sm-Co-Cu ternary system developed by Dai et al. [22]. As can be seen in Figure 3a, during the solidification process, the $\text{Sm}_2\text{Co}_{17}$ phase is precipitated firstly from the liquid phase of the $\text{Sm}_{12}\text{Co}_{88-x}\text{Cu}_x$ alloys with low Cu content (<24 at.%) and then the $\text{Sm}(\text{Co}, \text{Cu})_5$ phase is formed. In contrast, the α -Co phase is precipitated firstly from the liquid phase of the $\text{Sm}_{12}\text{Co}_{88-x}\text{Cu}_x$ alloys with high Cu content (>24 at.%) and then the $\text{Sm}_2\text{Co}_{17}$ and $\text{Sm}(\text{Co}, \text{Cu})_5$ phases are formed. In Figure 3b, it was found that the calculated volume fractions of the formed phases as a function of Cu substitution are consistent with the experimental results determined by the Rietveld refinements as shown in Table 1. The $\text{Sm}_5\text{Co}_{19}$ phase formed in the $\text{Sm}_{12}\text{Co}_{88-x}\text{Cu}_x$ as-cast alloys would change to the Sm_2Co_7 phase with the increase in Cu substitution, while the stable $\text{Sm}(\text{Co}, \text{Cu})_5$ phase is formed and the Sm_2Co_7 phase disappears. Meanwhile, the volume fraction of the $\text{Sm}_2\text{Co}_{17}$ phase decreases, while that of the $\text{Sm}(\text{Co}, \text{Cu})_5$ phase decreases. The formation of $\text{Sm}_5\text{Co}_{19}$ and Sm_2Co_7 phases in the $\text{Sm}_{12}\text{Co}_{88-x}\text{Cu}_x$ as-cast alloys is inhibited with the increase in Cu substitution, which is effective for the formation of the $\text{Sm}(\text{Co}, \text{Cu})_5$ phase in as-cast alloys.

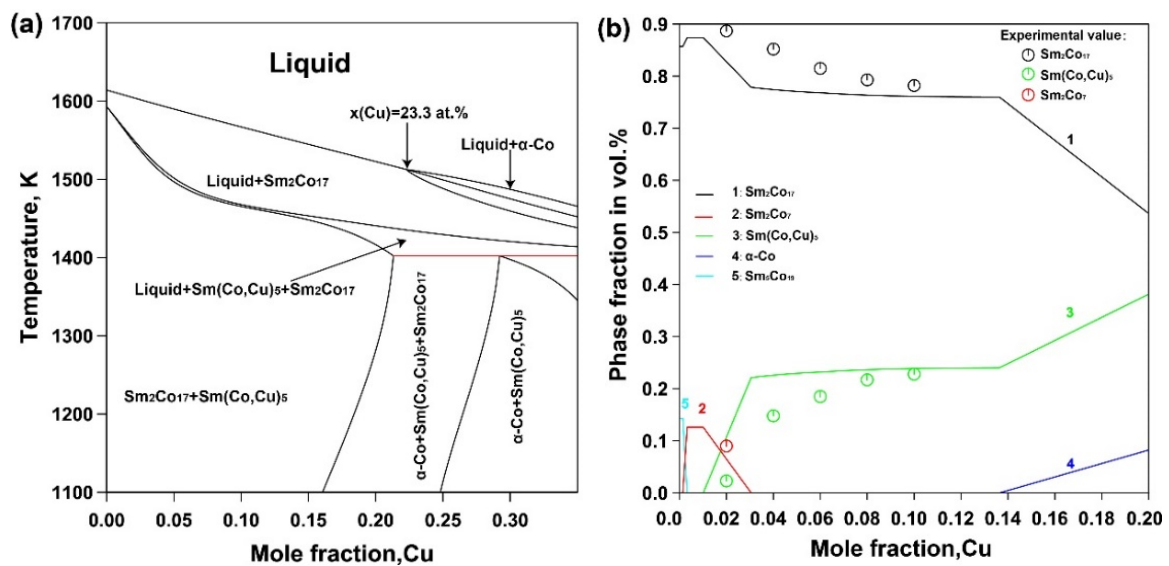


Figure 3. (a) Calculated vertical section of 12 at.% Sm in the Sm-Co-Cu ternary system and (b) calculated phase fractions as a function of Cu content in $\text{Sm}_{12}\text{Co}_{88-x}\text{Cu}_x$ as-cast alloys at 673 K.

Figure 4 is the Rietveld refinements of the XRD powder patterns of $\text{Sm}_{12}\text{Co}_{88-x}\text{Cu}_x$ ($x = 0, 2, 4, 6, 8, 10$) melt-spun ribbons. The lattice parameters, cell volumes and volume fractions of the formed phases in the $\text{Sm}_{12}\text{Co}_{88-x}\text{Cu}_x$ melt-spun ribbons obtained by the Rietveld refinements are given in Table 1. In Figure 4a, the ribbons show a single SmCo_7 phase, and the ribbons annealed at 1023 K for 1 h are still a single SmCo_7 phase in Figure 4b. For melt-spun ribbons and the melt-spun annealed at 1023 K, it can be seen from Table 1 that the lattice parameters and cell volumes of the ribbons with $x = 2, 4, 6, 8, 10$ are greater than the ribbon with $x = 0$. It means that Cu atoms with larger radius enter into the structure lattice of the SmCo_7 phase for replacing Co atoms in the $\text{Sm}_{12}\text{Co}_{88-x}\text{Cu}_x$ melt-spun ribbons and the $\text{Sm}_{12}\text{Co}_{88-x}\text{Cu}_x$ melt-spun ribbons annealed at 1023 K. Figure 4c exhibits that the ribbons annealed at 1123 K and 673 K show the formation of the $\text{Sm}_2\text{Co}_{17}$ and $\text{Sm}(\text{Co}, \text{Cu})_5$ phases, and the disappearance of the SmCo_7 phase. It was found that $\text{Sm}_{12}\text{Co}_{88-x}\text{Cu}_x$ ($x = 0, 2$) melt-spun ribbons are a single $\text{Sm}_2\text{Co}_{17}$ phase, while $\text{Sm}_{12}\text{Co}_{88-x}\text{Cu}_x$ (4, 6, 8, 10) melt-spun ribbons are composed of $\text{Sm}_2\text{Co}_{17}$ and $\text{Sm}(\text{Co}, \text{Cu})_5$ phases. Furthermore, the volume fraction of the $\text{Sm}(\text{Co}, \text{Cu})_5$ phase in the ribbons annealed at 1123 K and 673 K increases with the increase in Cu substitution, while that of the $\text{Sm}_2\text{Co}_{17}$ phase decreases. Furthermore, the lattice parameters and cell volumes of $\text{Sm}_2\text{Co}_{17}$ phases formed in $\text{Sm}_{12}\text{Co}_{88-x}\text{Cu}_x$ ribbons annealed at 1123 K and 673 K increase generally with the increase in Cu substitution, indicating that Cu atoms with larger radii enter the structure lattice of the $\text{Sm}_2\text{Co}_{17}$ phase for replacing Co atoms.

3.2. Magnetic Properties

Figure 5 shows the hysteresis loops of the $\text{Sm}_{12}\text{Co}_{88-x}\text{Cu}_x$ ($x = 0, 2, 4, 6, 8, 10$) melt-spun ribbons. Based on the hysteresis loops (M-H curves) as shown in Figure 5, the remanence (B_r) and coercivity (H_{cj}) of the ribbons were obtained, and the maximal magnetic energy product ($(BH)_{max}$) was determined as the area of the biggest rectangle that is inscribed in the second quadrant of B-H curves transformed from M-H curves. The magnetic properties (B_r , H_{cj} and $(BH)_{max}$) of the $\text{Sm}_{12}\text{Co}_{88-x}\text{Cu}_x$ ribbons determined in this work are summarized in Table 3 as shown in Figure 6. Figure 6a shows the B_r of the ribbons; the ribbons annealed at 1123 K and 673 K increase normally with the increase in Cu substitution, while that of the ribbons annealed at 1023 K increases and then decreases. In Figure 6b,c, the H_{cj} and $(BH)_{max}$ of the ribbons show similar tendencies with the increase in Cu substitution. The reason for it could be that the formation of the SmCo_5 phase in Sm-Co alloys can enhance the pinning effect of domain walls, and improve the magnetic properties

of the alloys, which was reported by Xu et al. [18], Cao et al. [23] and Xia et al. [24]. The XRD results in Figure 4c show that the $\text{Sm}(\text{Co}, \text{Cu})_5$ phase is formed in the $\text{Sm}_{12}\text{Co}_{88-x}\text{Cu}_x$ ($x = 4, 6, 8, 10$) ribbons annealed at 1123 K and 673 K. Furthermore, the volume fraction of the $\text{Sm}(\text{Co}, \text{Cu})_5$ phase in the ribbons annealed at 1123 K and 673 K increases with the increase in Cu substitution. The increase in the volume fraction of the $\text{Sm}(\text{Co}, \text{Cu})_5$ phase is an important factor for the significant increase in the H_{cj} and $(BH)_{\max}$ of the ribbons annealed at 1123 K and 673 K.

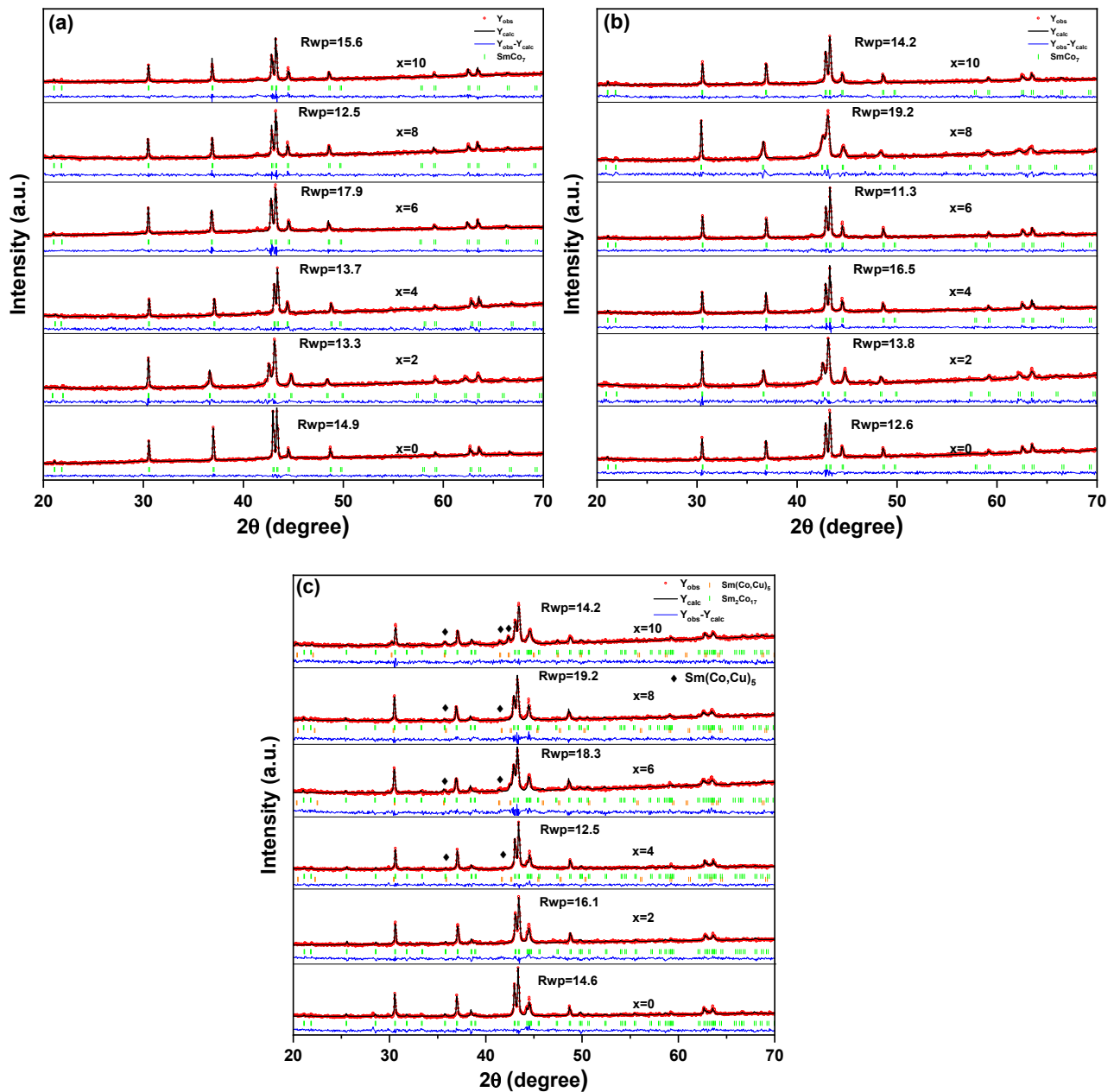


Figure 4. Rietveld refinements of XRD patterns of $\text{Sm}_{12}\text{Co}_{88-x}\text{Cu}_x$ ($x = 0, 2, 4, 6, 8, 10$) melt-spun ribbons. (a) Melt-spun ribbons, (b) Melt-spun ribbons annealed at 1023 K, (c) Melt-spun ribbons annealed at 1123 K and 673 K.

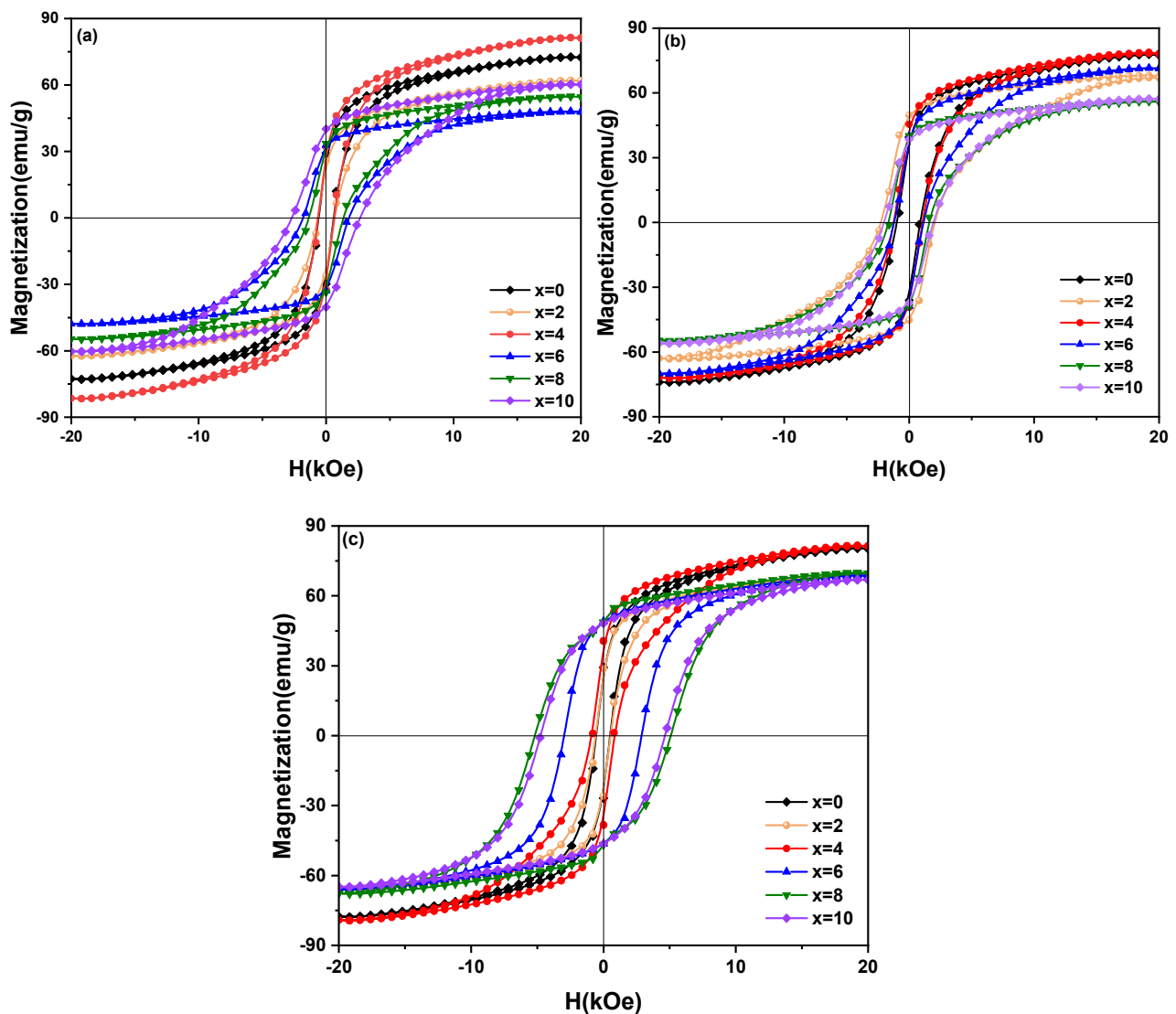


Figure 5. Hysteresis loops (M-H curves) of $\text{Sm}_{12}\text{Co}_{88-x}\text{Cu}_x$ ($x = 0, 2, 4, 6, 8, 10$) melt-spun ribbons with different heat treatments. (a) Melt-spun ribbons, (b) Melt-spun ribbons annealed at 1023 K, (c) Melt-spun ribbons annealed at 1123 K and 673 K.

Compared with the magnetic properties of the ribbons under different heat treatments in Figure 6, it was found that the B_r , H_{cj} and $(BH)_{\max}$ of the $\text{Sm}_{12}\text{Co}_{88-x}\text{Cu}_x$ ($x = 0, 2$) ribbons annealed at 1023 K are better than those of the unannealed ribbons. This could be due to the fact that the alloy composition and microstructure are much more uniform after heat treatment. However, after annealing at 1023 K, the magnetic properties of the $\text{Sm}_{12}\text{Co}_{88-x}\text{Cu}_x$ ($x = 6, 8, 10$) decreased. This could be due to the excessively large grain size and microstructure deterioration resulting in the reduction in remanence and coercivity during excessive heat treatment at a high temperature, which is similar to the results of Feng et al. [25]. In particular, after being annealed at 1123 K and 673 K, the B_r , H_{cj} and $(BH)_{\max}$ of $\text{Sm}_{12}\text{Co}_{88-x}\text{Cu}_x$ ($x = 6, 8, 10$) ribbons with high Cu content are much better, and increase generally with the increase in Cu substitution. The $\text{Sm}_{12}\text{Co}_{88-x}\text{Cu}_x$ ($x = 2$) ribbon annealed at 1023 K presents optimal magnetic properties ($B_r = 6.91$ kGs, $H_{cj} = 2.28$ kOe, $(BH)_{\max} = 3.86$ MGOe), while the best magnetic properties ($B_r = 6.76$ kGs, $H_{cj} = 5.20$ kOe and $(BH)_{\max} = 6.85$ MGOe) of the $\text{Sm}_{12}\text{Co}_{88-x}\text{Cu}_x$ ($x = 8$) ribbons annealed at 1123 K and 673 K were obtained in this work. Therefore, the magnetic properties of $\text{Sm}_{12}\text{Co}_{88-x}\text{Cu}_x$ ribbons determined in this work as a function of Cu substitution indicate that the heat

treatment is a promising and effective way to enhance the magnetic properties of Sm-Co-Cu melt-spun ribbons.

Table 3. Magnetic properties of $\text{Sm}_{12}\text{Co}_{88-x}\text{Cu}_x$ melt-spun ribbons.

$\text{Sm}_{12}\text{Co}_{88-x}\text{Cu}_x$ Ribbons	x	B_r (kGs)	H_{c1} (kOe)	$(BH)_{\max}$ (MGOe)
Melt-spun ribbons	0	4.06	0.57	0.43
	2	3.58	0.68	0.46
	4	4.41	0.62	0.58
	6	4.58	1.81	1.34
	8	4.67	1.37	1.14
	10	5.58	2.70	2.81
Melt-spun ribbons annealed at 1023 K	0	5.50	0.99	1.05
	2	6.91	2.28	3.86
	4	6.33	1.27	1.68
	6	5.63	1.21	1.52
	8	5.59	1.67	2.19
	10	5.34	2.03	2.44
Melt-spun ribbons annealed at 1123 K and 673 K	0	4.06	0.54	0.47
	2	4.12	0.60	0.53
	4	5.61	0.93	0.94
	6	6.82	2.98	5.88
	8	6.76	5.20	6.85
	10	6.70	4.77	6.72

In order to understand further the magnetization behavior of the ribbons, the initial magnetization curves and the first derivatives of the initial magnetization curve of $\text{Sm}_{12}\text{Co}_{88-x}\text{Cu}_x$ ribbons was measured at room temperature as shown in Figure 7. In Figure 7a, the initial magnetization of $\text{Sm}_{12}\text{Co}_{88-x}\text{Cu}_x$ ribbons increases rapidly with the increase in the external magnetic field, implying that the magnetization process of the ribbons is controlled by nucleation. It can be seen from Figure 7b that only one magnetization inversion exists in all the ribbons. Combined with the results of Figure 4a, the ribbons consist of SmCo_7 single phase, indicating that the magnetization process of $\text{Sm}_{12}\text{Co}_{88-x}\text{Cu}_x$ ribbons is controlled by a pure nucleation mechanism. In Figure 7c,d, the magnetization process of the $\text{Sm}_{12}\text{Co}_{88-x}\text{Cu}_x$ ribbons annealed at 1023 K is still controlled through pure nucleation. Figure 7e exhibits that the magnetization process of the $\text{Sm}_{12}\text{Co}_{88-x}\text{Cu}_x$ ($x = 0, 2, 4$) ribbons annealed at 1123 K and 673 K increases rapidly with the increase in the external magnetic field. Figure 7f shows that only one magnetization inversion exists in $\text{Sm}_{12}\text{Co}_{88-x}\text{Cu}_x$ ($x = 0, 2, 4$) ribbons annealed at 1123 K and 673 K, indicating that the magnetization process of the ribbons with low Cu content is controlled by pure nucleation. Nevertheless, there are two types of collective magnetization reversal in the initial magnetization curves of $\text{Sm}_{12}\text{Co}_{88-x}\text{Cu}_x$ ($x = 6, 8, 10$) ribbons annealed at 1123 K and 673 K in Figure 7e, indicating that the initial magnetization process of these ribbons with high Cu substitution is controlled by both pinning mechanism and nucleation. As can be seen in Figure 7f, when the external magnetic field is low, the local nucleation in $\text{Sm}_{12}\text{Co}_{88-x}\text{Cu}_x$ ($x = 6, 8, 10$) ribbons may be caused by direct contact of the $\text{Sm}_2\text{Co}_{17}$ phase. With the increase in the $\text{Sm}(\text{Co}, \text{Cu})_5$ phase, the domain wall pinning provided by the $\text{Sm}(\text{Co}, \text{Cu})_5$ phase ultimately determines the magnetization inversion of the $\text{Sm}_{12}\text{Co}_{88-x}\text{Cu}_x$ ($x = 6, 8, 10$) ribbons. It means that the coercivity mechanism of the ribbons annealed at 1123 K and 673 K changes from the nucleation mechanism to the pinning mechanism with the increase in Cu substitution.

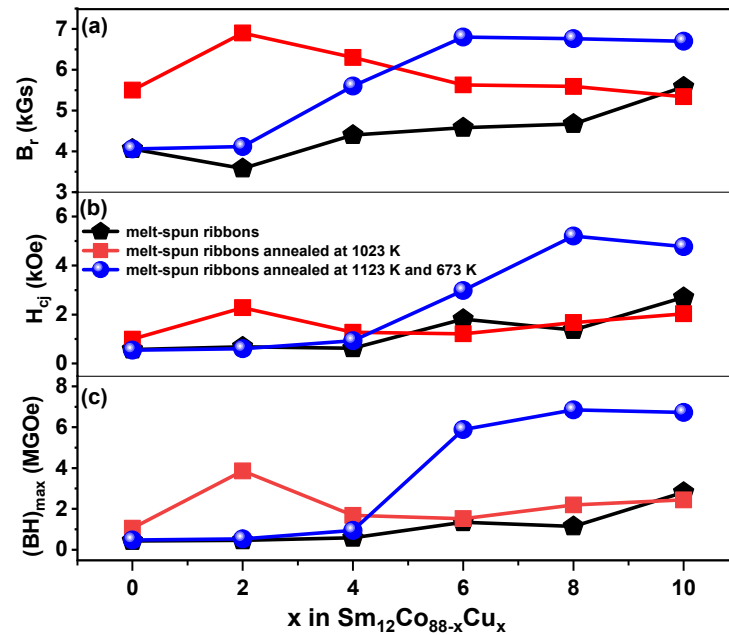


Figure 6. Magnetic properties as a function of Cu content in Sm₁₂Co_{88-x}Cu_x (x = 0, 2, 4, 6, 8, 10) melt-spun ribbons. (a) Melt-spun ribbons, (b) Melt-spun ribbons annealed at 1023 K, (c) Melt-spun ribbons annealed at 1123 K and 673 K.

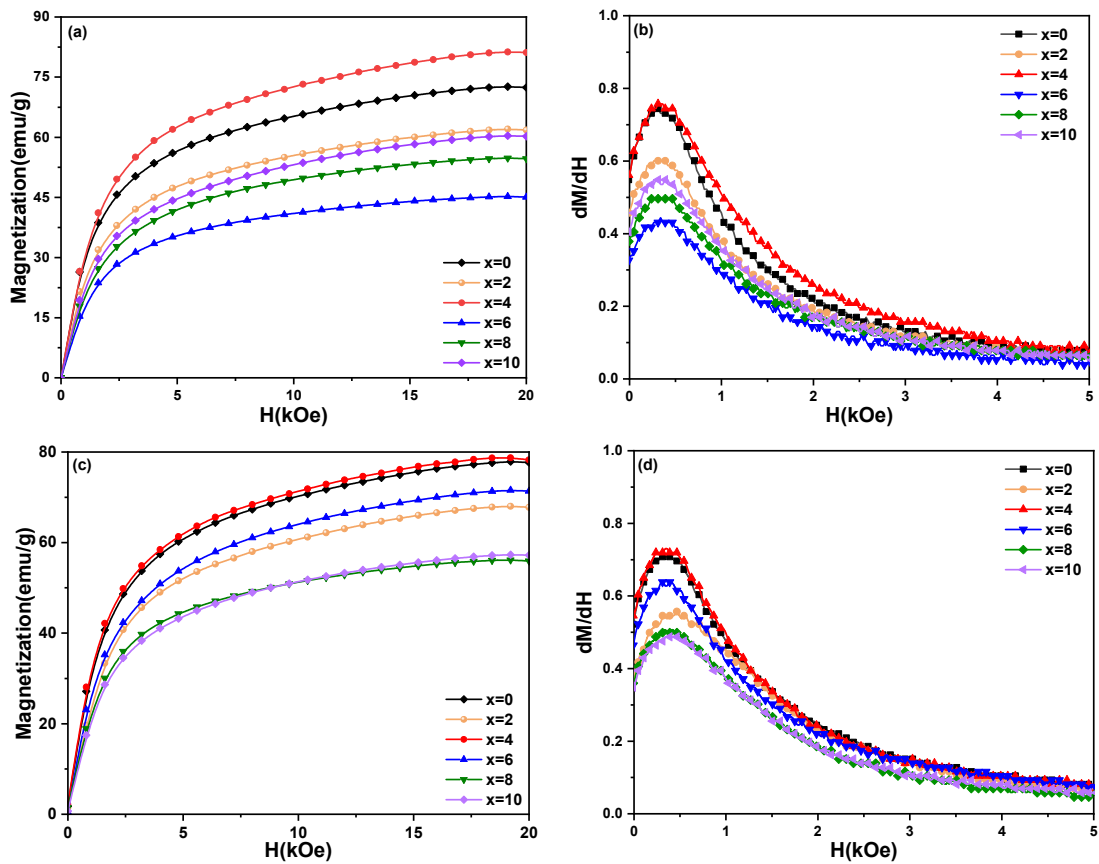


Figure 7. Cont.

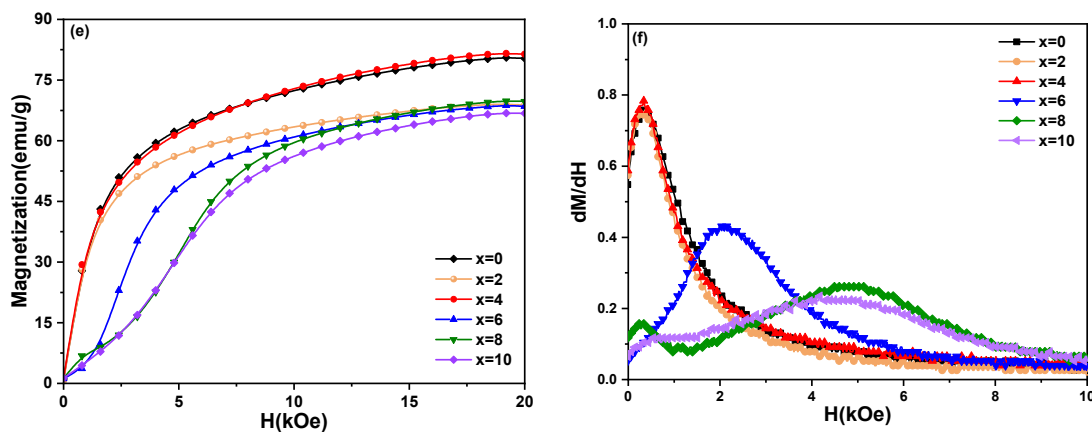


Figure 7. (a,c,e) The initial magnetization curves and (b,d,f) the first derivatives of the initial magnetization curve of $\text{Sm}_{12}\text{Co}_{88-x}\text{Cu}_x$ ($x = 0, 2, 4, 6, 8, 10$) melt-spun ribbons with different heat treatments. (a,b) Melt-spun ribbons, (c,d) Melt-spun ribbons annealed at 1023 K, (e,f) Melt-spun ribbons annealed at 1123 K and 673 K.

4. Conclusions

The effects of Cu substitution and heat treatment on the phase formation and magnetic properties of $\text{Sm}_{12}\text{Co}_{88-x}\text{Cu}_x$ melt-spun ribbons were investigated in this work using XRD, SEM-EDS and VSM. The following conclusions could be drawn:

- (1) The XRD and SEM-EDS results indicate that the $\text{Sm}_{12}\text{Co}_{88-x}\text{Cu}_x$ ($x = 0$) as-cast alloy contains $\text{Sm}_2\text{Co}_{17}$ and $\text{Sm}_5\text{Co}_{19}$ phases, and the $\text{Sm}_{12}\text{Co}_{88-x}\text{Cu}_x$ ($x = 2$) as-cast alloy is composed of $\text{Sm}_2\text{Co}_{17}$, Sm_2Co_7 and $\text{Sm}(\text{Co}, \text{Cu})_5$ phases. Both the $\text{Sm}_2\text{Co}_{17}$ and $\text{Sm}(\text{Co}, \text{Cu})_5$ phases are detected in the $\text{Sm}_{12}\text{Co}_{88-x}\text{Cu}_x$ ($x = 4, 6, 8, 10$) as-cast alloys. Meanwhile, $\text{Sm}_{12}\text{Co}_{88-x}\text{Cu}_x$ ribbons show a single SmCo_7 phase, which is still formed in the ribbons annealed at 1023 K. After being annealed at 1123 K and 673 K, $\text{Sm}_{12}\text{Co}_{88-x}\text{Cu}_x$ ($x = 0, 2$) ribbons consist of a $\text{Sm}_2\text{Co}_{17}$ single phase, while $\text{Sm}_{12}\text{Co}_{88-x}\text{Cu}_x$ ($x = 4, 6, 8, 10$) ribbons contain $\text{Sm}_2\text{Co}_{17}$ and $\text{Sm}(\text{Co}, \text{Cu})_5$ phases.
- (2) Magnetic measurements show that the magnetic properties of $\text{Sm}_{12}\text{Co}_{88-x}\text{Cu}_x$ ribbons ($x = 4, 6, 8, 10$) with high Cu substitution annealed at 1123 K and 673 K are improved significantly, and the coercivity mechanism of these ribbons is controlled by both a pinning mechanism and a nucleation mechanism. The volume fraction of the $\text{Sm}(\text{Co}, \text{Cu})_5$ phase in the ribbons increases after heat treatment, which is an important factor for the enhancement of the coercivity and maximal magnetic energy product. The best magnetic properties with $B_r = 6.76$ kGs, $H_{c_j} = 5.20$ kOe and $(\text{BH})_{\text{max}} = 6.85$ MGOe were achieved in $\text{Sm}_{12}\text{Co}_{88-x}\text{Cu}_x$ ($x = 8$) ribbons annealed at 1123 K and 673 K.

Author Contributions: Data curation, F.D., P.L., L.L. and D.C.; Formal analysis, P.L., L.L. and D.C.; Funding acquisition, J.W.; Investigation, F.D.; Methodology, L.L.; Project administration, J.W.; Resources, Q.Y.; Supervision, J.W.; Writing—original draft, F.D. and P.L.; Writing—review & editing, Q.Y. and J.W. All authors have read and agreed to the published version of the manuscript.

Funding: This work was supported financially by National Natural Science Foundation of China (51971069), Guangxi Natural Science Foundation (2020GXNSFFA297004), Guangxi Key Laboratory of Information Materials (211007-Z) and Engineering Research Center of Electronic Information Materials and Devices (EIMD-AA202004), Guilin University of Electronic Technology, China. The authors thank the support from the foundation for Guangxi Bagui scholars.

Institutional Review Board Statement: Not applicable.

Informed Consent Statement: Not applicable.

Data Availability Statement: Data sharing is not applicable to this article.

Conflicts of Interest: The authors declare no conflict of interest.

References

1. Coey, J. Hard magnetic materials: A perspective, magnetics. *IEEE Trans. Magn.* **2011**, *47*, 4671–4681. [[CrossRef](#)]
2. Gutfleisch, O.; Willard, M.A.; Brück, E.; Chen, C.H.; Sankar, S.G.; Liu, J.P. Magnetic materials and devices for the 21st century: Stronger, lighter, and more energy efficient. *Adv. Mater.* **2011**, *20*, 1–22. [[CrossRef](#)] [[PubMed](#)]
3. Poudyal, N.; Liu, J.P. Advances in nanostructured permanent magnets research. *J. Phys. D Appl. Phys.* **2013**, *46*, 043001. [[CrossRef](#)]
4. Schobinger, D.; Gutfleisch, O.; Hinz, D.; Muller, K.H.; Schultz, L.; Martinek, G. High temperature magnetic properties of 2:17 Sm-Co magnets. *J. Magn. Magn. Mater.* **2002**, *242*, 1347–1349. [[CrossRef](#)]
5. Al-Omari, I.A.; Skomski, R.; Thomas, R.A.; Leslie-Pelecky, D.; Sellmyer, D.J. High-temperature magnetic properties of mechanically alloyed SmCo₅ and YCo₅ magnets. *IEEE Trans. Magn.* **2001**, *37*, 2534–2536. [[CrossRef](#)]
6. Zhang, C.Y.; Liu, Z.; Li, M.; Liu, L.; Li, T.Y.; Chen, R.J.; Lee, D.; Yan, A. The evolution of phase constitution and microstructure in iron-rich 2:17-type Sm-Co magnets with high magnetic performance. *Sci. Rep.* **2018**, *8*, 9103. [[CrossRef](#)]
7. Sepehri-Amin, H.; Fischbacher, J.; Ohkubo, T.; Schrefl, T.; Gutfleisch, O.; Hono, K. Correlation of microchemistry of cell boundary phase and interface structure to the coercivity of Sm(Co_{0.784}Fe_{0.100}Cu_{0.088}Zr_{0.028})_{7.19} sintered magnets. *Acta Mater.* **2017**, *126*, 1–10. [[CrossRef](#)]
8. Chen, H.S.; Wang, Y.Q.; Yao, Y.; Qu, J.T.; Yun, F.; Li, Y.Q.; Ringer, S.P.; Yue, M.; Zheng, R.K. Attractive-domain-wall-pinning controlled Sm-Co magnets overcome the coercivity-remance trade-off. *Acta Mater.* **2019**, *164*, 196–206. [[CrossRef](#)]
9. Zhu, G.J.; Lou, L.; Song, W.P.; Zhang, Q.; Hua, Y.X.; Huang, G.W.; Li, X.H.; Zhang, X.Y. Development of crystallography texture in SmCo₇/α-Fe nanocomposite magnets prepared by high-pressure thermal compression. *J. Alloys Compd.* **2018**, *750*, 414–419. [[CrossRef](#)]
10. Urzhumtsev, A.; Maltseva, V.; Volegov, A. Magnetization reversal processes in sintered permanent magnets Sm(Co, Fe, Zr, Cu)_z. *J. Magn. Magn. Mater.* **2022**, *551*, 169143. [[CrossRef](#)]
11. Cao, J.; Zhang, T.L.; Xu, H.; Liu, J.H.; Hu, M.Y.; Xi, L.L.; Wang, H.; Jiang, C.B. Exploring microstructural origin of squareness-coercivity trad-off in iron-rich Sm-Co-Fe-Cu-Zr magnets. *Scr. Mater.* **2022**, *209*, 114418. [[CrossRef](#)]
12. Yao, Q.; Liu, W.; Zhao, X.G.; Zhang, Z.D. Structure and magnetic properties of Cu-doped SmCo_{6.7-x}Cu_xCr_{0.3} magnets. *J. Appl. Phys.* **2007**, *102*, 093905. [[CrossRef](#)]
13. Shang, Z.F.; Zhang, D.T.; Xie, Z.H.; Wang, Y.Q.; Haseeb, M.; Qiao, P.B.; Liu, W.Q.; Yue, M. Effects of copper and zirconium contents on microstructure and magnetic properties of Sm(Co,Fe,Cu,Zr)_z magnets with high iron content. *J. Rare Earths* **2021**, *39*, 160–166. [[CrossRef](#)]
14. Téllez-Blanco, J.C.; Grössinger, R.; Turtelli, R.S. Structure and magnetic properties of SmCo_{5-x}Cu_x alloys. *J. Alloys Compd.* **1998**, *281*, 1–5. [[CrossRef](#)]
15. Horiuchi, Y.; Hagiwara, M.; Okamoto, K.; Kobayashi, T. Effects of solution treated temperature on the structural and magnetic properties of iron-rich Sm(CoFeCuZr)_z sintered magnet. *IEEE Trans. Magn.* **2013**, *49*, 3221–3224. [[CrossRef](#)]
16. Horiuchi, Y.; Hagiwara, M.; Endo, M.; Sanada, N.; Sakurada, S. Influence of intermediate-heat treatment on the structure and magnetic properties of iron-rich Sm(CoFeCuZr)_z sintered magnets. *J. Appl. Phys.* **2015**, *117*, 17C704.1–17C704.4. [[CrossRef](#)]
17. Wang, Y.Q.; Yue, M.; Wu, D.; Zhang, D.T.; Liu, W.Q.; Zhang, H.G.; Du, Y.H. Effect of Cu redistribution in grain boundary on magnetic properties of Sm(Co_{0.665}Fe_{0.25}Cu_{0.06}Zr_{0.025})₇ permanent magnets. *J. Alloys Compd.* **2018**, *741*, 495–500. [[CrossRef](#)]
18. Xu, C.; Wang, H.; Liu, B.J.; Xu, H.; Zhang, T.L.; Liu, J.H.; Jiang, C.B. The formation mechanism of 1:5H phase in Sm(Co,Fe,Cu,Zr)_z melt-spun ribbons with high iron content. *J. Magn. Magn. Mater.* **2020**, *496*, 165939. [[CrossRef](#)]
19. Guo, Y.Q.; Li, W.; Feng, W.C. Structural stability and magnetic properties of SmCo_{7-x}Ga_x. *Appl. Phys. Lett.* **2005**, *86*, 192513. [[CrossRef](#)]
20. Chang, H.W.; Huang, S.T.; Chang, C.W. Effect of C addition on the magnetic properties, phase evolution, and microstructure of melt-spun SmCo_{7-x}Hf_x (x = 0.1–0.3) ribbons. *Solid State Commun.* **2008**, *147*, 69–73. [[CrossRef](#)]
21. Yuan, Y.; Yi, J.H.; Borzone, G.; Watson, A. Thermodynamic modeling of the Co-Sm system. *Calphad* **2011**, *35*, 416. [[CrossRef](#)]
22. Dai, F.L.; Liu, P.P.; Luo, L.; Chen, D.K.; Yao, Q.R.; Wang, J.; Rao, G.H.; Zhou, H.Y. Experimental investigation and thermodynamic modeling of the Sm-Co-Cu ternary system. *Calphad* **2022**. submitted.
23. Cao, J.; Zhang, T.; Liu, J.; Xu, H.; Jiang, C. Grain boundary optimization induced substantial squareness enhancement and high performance in iron-rich Sm-Co-Fe-Cu-Zr magnets. *J. Mater. Sci. Tech.* **2021**, *85*, 56–61. [[CrossRef](#)]
24. Xia, W.; Zhang, T.L.; Liu, J.H.; Dong, Y.; Wang, H.; Jiang, C.B. Influence of the final heat treatment temperature on the magnetic property losses of Sm(Co,Fe,Cu,Zr)_z high temperature magnets. *J. Magn. Magn. Mater.* **2021**, *528*, 167763. [[CrossRef](#)]
25. Feng, D.Y.; Liu, Z.W.; Zheng, Z.G.; Zeng, D.C.; Zhang, G.Q. The structure, anisotropy and coercivity of rapidly quenched TbCu₇-type SmCo_{7-x}Zr_x alloys and the effects of post-treatments. *J. Magn. Magn. Mater.* **2013**, *347*, 18–25. [[CrossRef](#)]